Nanoscale

PAPER

View Article Online
View Journal | View Issue

Cite this: *Nanoscale*, 2025, **17**, 22349

A flexible tactile sensor with decoupled multimodal sensing capacity based on melamine sponge-MXene@CsPbBr$_3$ aerogel

Ying Cao,†[a,b] Shihao Deng,†[a,b] Shuang Xia,[a,b] Ju Bai,[b] Shen Yuan,[b] Ting Zhang *[a,b] and Tie Li *[a,b,c]

Received 8th July 2025,
Accepted 2nd September 2025

DOI: 10.1039/d5nr02882e

rsc.li/nanoscale

Humanoid robots, as well as the requirement for sensing force and temperature, are at high risk of prolonged exposure to complex light conditions, especially UV radiation in automotive baking workshops, outer space, *etc.*, which will make the circuits and electronic components extremely prone to aging, necessitating timely assessment. Here, a multimodal flexible tactile sensor is assembled by utilizing a novel melamine sponge-MXene@CsPbBr$_3$ hybrid aerogel as the sensing unit, whereby the melamine sponge provides the deformable support skeleton, the MXene realizes the functions of piezoresistive pressure sensing and thermoelectric temperature detecting, and the CsPbBr$_3$ realizes not only the light-sensing behavior, especially the visual capacity of ultraviolet excited photoluminescence, but also the synergetic enhancement of thermoelectric ability. *Via* these different kinds of sensing mechanisms, the derived flexible tactile sensor realizes multimodal response to pressure, temperature and ultraviolet without cross-coupling. Furthermore, by using a machine learning algorithm, it can distinguish the hardness and material of six automotive parts with high recognition accuracy of 98.2% and 98.6%, respectively. Moreover, based on the visual photoluminescence capability, a sensory array is assembled to successfully recognize different shapes. This work provides a feasible way to protect robots when used in complex operating environments.

1 Introduction

In recent years, intelligent equipment, such as humanoid robots, has been receiving more and more attention in various industrial and living scenarios,[1,2] but such equipment needs to have sufficient sensing capacities to accurately interact with the external environment.[3,4] Especially, the bionic tactile function analogous to human skin can endow them with the fine recognition ability of various materials, like hardness and texture,[5–7] which can be realized by a new type of sensor, *i.e.* a flexible tactile sensor, which possesses many advantages, such as conformal surface, lightweight, large area, and low cost.[8,9] Furthermore, with the rapid expansion of applications, the risk of prolonged exposure to complex light conditions, especially UV radiation, is increasing for intelligent equipment, such as in the automotive industry, the sterilization of medical devices, and outer space radiation, which will make the circuits and electronic components extremely prone to aging, necessitating timely assessment. As described above, the employment of flexible sensors with multimodal tactile sensing capability is also a reliable solution to practically solve the produced hazards. Unfortunately, most of the previously reported flexible sensors exhibit only a single sensing capability or provide similar output patterns for different external signals, such as temperature, pressure and light radiation. That is because the sensitive materials, which are the core units of the sensors, do not possess a high-selectivity response capability. Therefore, there is an urgent need to develop new multifunctional and interference-free sensitive composites that can realize the behaviors of flexible tactile sensors for long-term and stable operation in complex light radiation conditions, especially the UV radiation environment.

As is well-known, various sensitive materials, including carbonaceous graphene[10] and nanotubes,[11] polymers like PSS:PEDOT[12] and metal hybrids,[13] have been used to assemble various flexible tactile sensors, but they commonly respond only to a variety of signals and have no selective response be-

---

[a] *School of Nano-Tech and Nano-Bionics, University of Science and Technology of China, Hefei, Anhui, 230026, P.R. China. E-mail: tzhang2009@sinano.ac.cn, tli2014@sinano.ac.cn*

[b] *i-lab, Suzhou Institute of Nano-Tech & Nano-Bionics (SINANO), Chinese Academy of Sciences (CAS), Suzhou, Jiangsu, 215123, P. R. China*

[c] *Jiangxi Institute of Nanotechnology, 278 Luozhu Road; Xiaolan Economic and Technological Development Zone, Nanchang, 330200, China*

† These authors contributed equally to this work.

havior. For example, most carbonaceous-based flexible devices exhibit similar response outputs to temperature and pressure changes, leading to difficulties in decoupling the sensing signals. More importantly, it must be noted that most of these, like polymers, also lack the ability to operate under light radiation conditions, especially when exposed to UV radiation, nor do they respond to light radiation. In contrast, on the one hand, MXene, as a kind of two-dimensional material, possesses a high thermoelectric coefficient and mechanical properties, which can favor the high-selective temperature and pressure response behavior of its derived nanocomposites on account of two different sensing mechanisms of the passive thermoelectric outputs and the active piezoresistive variations.[14,15] On the other hand, $CsPbBr_3$, as a kind of highly stable perovskite, is a sensitive material with excellent optoelectronic properties, which can detect with high sensitivity low-band light for its appropriate bandwidth, and can even translate them into visible light bands.[16–18] Importantly, this light response behavior is almost unaffected by the variations of pressure and temperature. Therefore, it is anticipated that a valid composite of MXene and $CsPbBr_3$ would synchronously maintain their respective high-selective response abilities to pressure, temperature and light radiation, thus realizing the as-anticipated multisensory functions with decoupled capacity. Moreover, all components loading on a reliable substrate is also an effective solution to realize high stability for a nanocomposite.[19] Here, a dense melamine sponge is employed to load the as-obtained sensing matter composed of MXene and $CsPbBr_3$ to form a new-style sensitive hybrid aerogel, finally assembling it into a flexible tactile sensor. To the best of our knowledge, there are few studies that have reported this hybrid aerogel to sense pressure, temperature and light radiation independently.

Herein, in this study, a novel melamine sponge-MXene@$CsPbBr_3$ hybrid aerogel with a defined microstructural skeleton is fabricated *via* a dip-coating approach. In this structure, the robust melamine sponge serves as the mechanical support framework, while the MXene enables both pressure and temperature sensing behaviors. More importantly, the $CsPbBr_3$ not only exhibits light-sensing capabilities, particularly ultraviolet excited photoluminescence, but also contributes to the synergistic enhancement of thermoelectric performance. Furthermore, through three different sensing mechanisms of the piezoresistive response behavior, the non-stationary thermoelectric principle, and the photocurrent ability, this hybrid aerogel-derived flexible tactile sensor can detect the above parameters of pressure, temperature and light radiation without any cross-coupling. Ultimately, to verify the actual application performance, this flexible tactile device is employed to differentiate the hardness and material of objects used in automotive parts, showing high recognition accuracy of 98.2% and 98.6% *via* a decision tree algorithm, respectively. Furthermore, based on the visual photoluminescence function, a sensory array is assembled to successfully recognize different shapes. In brief, these inventions provide a new way to enable intelligent equipment to be more suitable for applications in complex conditions.

2 Results and discussion

2.1 Preparation and characterization of the hybrid aerogel

The preparation process for the melamine sponge-MXene@$CsPbBr_3$ hybrid aerogel is shown in Fig. S1. Specifically, a few layers of MXene nanosheets are firstly prepared by chemical stripping method. Then, the precursor solutions used for preparing $CsPbBr_3$ are added to the dimethylsulfoxide (DMSO) dispersion of MXene, which is thoroughly mixed at room temperature and repeatedly dipped into a dense melamine sponge, finally achieving the as-anticipated melamine sponge-MXene@$CsPbBr_3$ hybrid aerogel by vacuum drying process. In this process, the $CsPbBr_3$ nanosheets are obtained by the room-temperature solution growth strategy, which grows the nanosheets directly on the surface and interlayer of MXene nanosheets. Subsequently, a series of characterizations are performed to verify the physical phase and chemical composition of this product. In detail, the X-ray diffraction analysis of this aerogel displays all the characteristic peaks of MXene and $CsPbBr_3$ (Fig. 1a), which preliminarily verifies the reliability of this prepared methodology as well as the loaded hybrid with good crystallinity and structural ordering. Notedly, the characteristic peak of MXene is shifted to the left by 1.42°, indicating the increase of the corresponding layer spacing due to the embedding of smaller $CsPbBr_3$ nanosheets during the compositing process. Moreover, the X-ray photoelectron spectra (XPS) of the final aerogel and the corresponding TiO_2 peaks in MXene are also analyzed (Fig. 1b and c), which clearly demonstrates that no oxidation of MXene occurs even after the drying treatment at a temperature of 70 °C, showing its high environmental stability due to the effective interaction of the precursors. Moreover, Fourier transform infrared (FTIR) and Raman spectroscopy were used to investigate the interrelation between the active material and the matrix (Fig. S2a and b), showing the visible changes of the main peaks of the sponge (a small shift around the 1320 cm^{-1} and 1470 cm^{-1} peaks for the C═O and C–H vibration peaks in the FTIR spectra, and a significant decrease around the 1000 cm^{-1} peak for C═C skeleton peaks in the Raman spectra, respectively), which indicates the occurrence of intermolecular interactions on the sponge matrix. This will be beneficial for the enhanced stability of the final product.

In addition, a series of morphological characterizations are performed for the aerogel and its corresponding components. As shown in Fig. S3, the morphologies of the intermediates of MXene, $CsPbBr_3$ and MXene@$CsPbBr_3$, as well as their corresponding elemental distributions, all display the as-anticipated two-dimensional lamellar structure with uniform distribution of $CsPbBr_3$. Moreover, as shown in Fig. S4, the $CsPbBr_3$ nanosheet displays a thickness of 8 nm, and the thickness of the intermediate MXene@$CsPbBr_3$ is increased by about 5 nm after hybridisation with MXene, showing the successful compositing of the above lamellar structures. Furthermore, the final product presents a classical aerogel framework (Fig. 1d) and all the constituent elements are uniformly distributed therein (Fig. 1e), which will be favorable for enhancing the

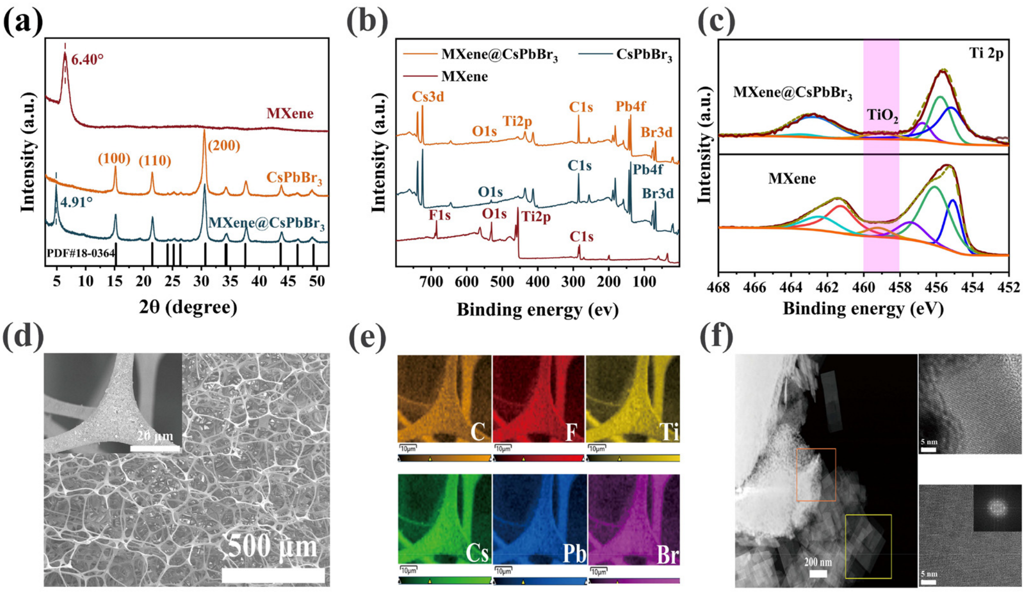

Fig. 1 Characterization of the melamine sponge-MXene@CsPbBr$_3$ aerogel. (a) XRD, (b) XPS and (c) Ti 2p analysis of the intermediate products of MXene, CsPbBr$_3$ and MXene@CsPbBr$_3$. The morphological (d) SEM, (e) element distribution mapping and (f) TEM results of the as-obtained hybrid aerogel.

mechanical loading and electron transfer behaviors. The microscopic morphology of the composite is further characterized by transmission electron microscope (TEM), as shown in Fig. 1f. The enlarged image of the orange box shows the effective composite of MXene and CsPbBr$_3$, and the yellow one shows that CsPbBr$_3$ has an obvious cubic crystal structure. In sum, these results clearly demonstrate the successful preparation of the as-anticipated melamine sponge-MXene@CsPbBr$_3$ hybrid aerogel with well-defined intrinsic architecture.

2.2 Intrinsic properties of the hybrid aerogel

Subsequently, a systematic test is carefully carried out to investigate the intrinsic performance of this melamine sponge-MXene@CsPbBr$_3$ aerogel, mainly containing the mechanical and thermoelectric properties, and the visual photoluminescence (PL) behavior. Firstly, the effect of CsPbBr$_3$ on the thermoelectric performance is tested and shown in Fig. 2a, revealing that, as well as the main contribution from MXene, the incorporation of CsPbBr$_3$ can significantly enhance the thermoelectric coefficient of the product. This can be ascribed to its intrinsic semi-conductive feature of the thermal field exciting carrier's behavior, as a result, more carriers participate in the formation of the built-in ion field, outputting enhanced thermoelectric voltage. Fig. 2b shows the physical image of the final product, revealing ultralight status, which is beneficial for obtaining higher relative mechanical properties. The stress–strain curves at different set strains of 0–90% (Fig. 2c and Fig. S5) reveal the excellent compression capacity of the aerogel; even after deformation at a strain of 90%, the aerogel can recover to its initial state after releasing the external pressure, exhibiting highly reversible compression at any applied strain condition. In addition, the product exhibits highly stable stress–strain properties under various compression rates of 20–300 mm min^{-1} (Fig. 2d) and good fatigue resistance during a long-term compression test of 1000 cycles (Fig. 2e) and a high temperature (Fig. S2c), indicating that its mechanical strength is independent of the rate of applied force and the ambient temperature, which is of great significance for the realization of aerogel-derived flexible sensors for practical applications.

Subsequently, due to the presence of CsPbBr$_3$ perovskite, the ultraviolet (325 nm) excited PL behavior of the melamine sponge-MXene@CsPbBr$_3$ aerogels with various ratios of components is explored, as shown in Fig. 2f. There is no obvious emission peak in the visible range for pure MXene, yet an emission peak was observed at 533 nm for both CsPbBr$_3$ and the derived aerogels, which is located in the wavelength band of green light. Moreover, the CsPbBr$_3$ is *in situ* loaded on the interlayer lamellar surface of the MXene, which leads to obvious changes of the luminescence intensity of the aerogels, of which the sample with the lowest MXene content shows the greatest PL intensity, indicating that this performance mainly depends on the CsPbBr$_3$ component, and a small amount of MXene can effectively enhance this appearance due to its rapid electron–hole separation capability as a semiconductor at this level. However, the excessive addition of MXene will gradually increase the conductivity, resulting in the reduction of the PL intensity, which can be proved by the reduced fluorescence lifetimes of the composites, as shown in Fig. S6. Moreover, combining with the obtained controlled results of the thermoelectric performance (Fig. S7), the optimal ratio of MXene and CsPbBr$_3$ for the final product is 1 : 62, which is chosen as the sample for all subsequent experiments.

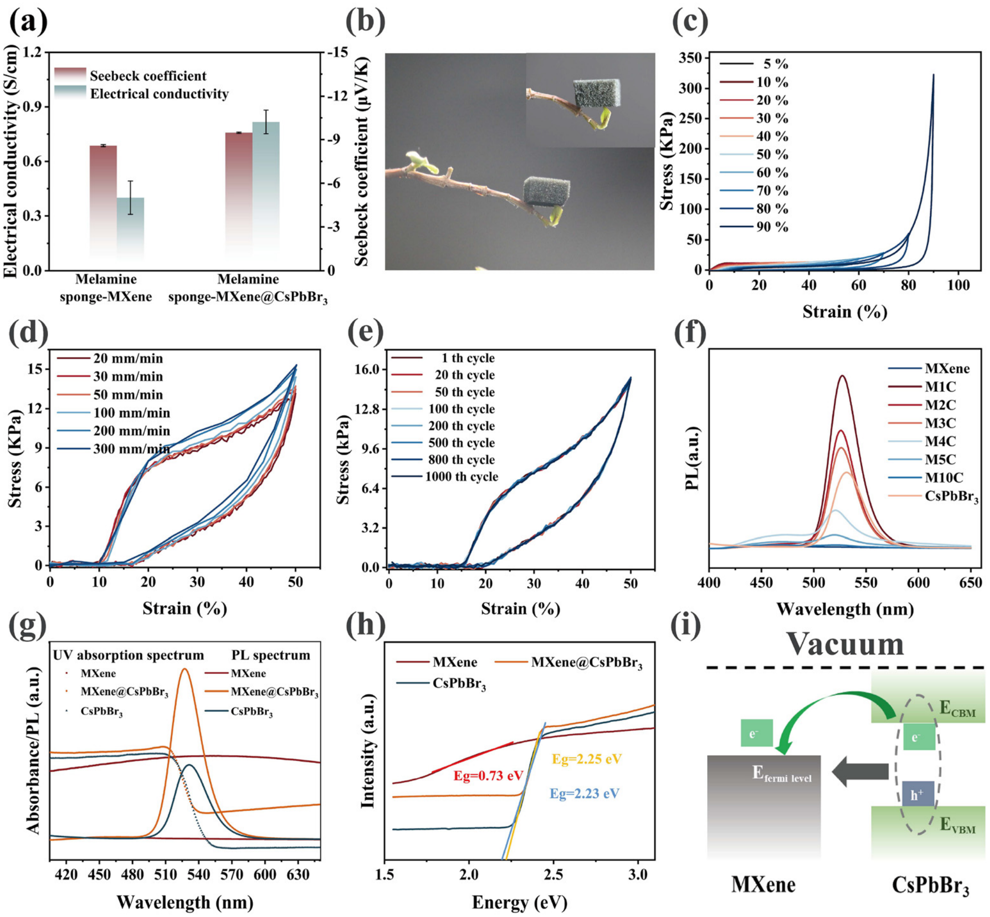

Fig. 2 Intrinsic properties of the melamine sponge-MXene@$CsPbBr_3$ aerogel. (a) Comparison of the conductivity and Seebeck coefficient of the composites with or without $CsPbBr_3$. (b) Image of the aerogel. The stress–strain (σ–ε) curve of the aerogel at different (c) set strains and (d) compression velocities. (e) The stability curves of the aerogel with the optimal ratio tested at a strain of 50% for 1000 compression cycles. (f) The ultraviolet excited photoluminescence (PL) properties of the aerogel with different compositions under 365 nm UV light; here *M* is the volume of MXene solution, for example, M1 means 1 mL of the original solution; and C is the content of $CsPbBr_3$ synthesized according to the original ratio. (g) The UV-absorption spectra and (h) the corresponding bandgap widths of MXene, $CsPbBr_3$ and MXene@$CsPbBr_3$, and (i) the schematic diagram energy transfer model.

To deeply analyze the effect of the composite of MXene and $CsPbBr_3$ on the PL performance, further UV-vis spectroscopic characterization is carried out, as shown in Fig. 2g. It can be seen that neither obvious luminescence peaks nor absorption peaks are displayed for MXene, whereas there are emission and absorption peaks in the green light band (533 nm) for the $CsPbBr_3$ nanosheets, while their corresponding composite also has the same characteristic peaks, and the intensity of its emission peaks is larger than that of the $CsPbBr_3$ nanosheets, which is mainly due to the effective charge or energy transfer between the $CsPbBr_3$ nanosheets grown directly on top of the MXene nanosheets. Furthermore, the bandgaps are calculated based on their UV-vis spectroscopy *via* the following eqn (1):[20]

$$\frac{\alpha \times h\nu}{m} = B \times (h\nu - E_g) \tag{1}$$

where m = 1/2 for the direct bandgap, α is the absorption coefficient, B is a constant, $h\nu$ is the photon energy (h is Planck's constant, and ν is the incident photon frequency), and E_g denotes the bandgap width. As shown in Fig. 2h, the MXene, pure $CsPbBr_3$ and their corresponding MXene@$CsPbBr_3$ composite in the aerogel reveal direct bandgaps of 0.73 eV, 2.23 eV and 2.25 eV, respectively, further verifying that the fluorescence behavior is unaffected by the MXene. Furthermore, the UV photoelectron spectroscopy of the MXene and $CsPbBr_3$ components in the aerogel is carried out (Fig. S8), and the Fermi energy level of MXene is about 4.98 eV, whereas the valence band maxima (VBM) and the conduction band minima (CBM) for $CsPbBr_3$ are located at about 5.42 eV and 2.7 eV, respectively, which are consistent with previous reports. According to the Marcus electron transfer theory, it is unfavorable to achieve charge transfer at larger energy differences because more phonons are required in this process. Therefore, the energy difference between the Fermi energy levels of MXene and $CsPbBr_3$ is small, and therefore the probability of electron transfer from $CsPbBr_3$ to MXene is greater compared to hole transfer. Based on this, the energy transfer of MXene@$CsPbBr_3$ is modeled and shown in Fig. 2i, where the electrons and holes are generated in $CsPbBr_3$ under UV excitation (325 nm), and they can transfer to MXene through the heterointerface to achieve a more efficient separation of the electrons and holes, resulting in enhanced luminescence performance. In brief, the as-prepared MXene@$CsPbBr_3$ aerogel shows favorable intrinsic comprehensive performance, including the conductivity, mechanical and ultraviolet (325 nm) excited PL properties.

2.3 Pressure-sensing performance of the flexible sensor

The piezoresistive sensing behavior of the melamine sponge-MXene@$CsPbBr_3$-derived flexible sensor is systematically investigated, as shown in Fig. 3. From the mechanism schematic in Fig. 3a, the resistance variation of this flexible sensor is mainly due to the change of the contact area inside the aerogel with compression deformation. When the pressure causes stress to increase, the conductive network is reconstructed, the contact between neighboring networks increases synchronously, and the contact resistance tends to decrease rapidly, and the sensitivity of this compression process is 0.559 kΩ kPa^{-1}, as shown in Fig. 3b. In addition, the response time is also an important indicator for a sensor, with our sensor displaying response and recovery times of about 1 s and 0.6 s, respectively (Fig. 3c). Moreover, the cycling performance of this flexible sensor under different stresses (Fig. 3d) and rates (Fig. 3e) is also explored, showing excellent cycling stability and repeatability at all stages of stress and rate, which indicates that the device can detect external pressure without being subject to an external contact rate. On the other hand, the initial design of this flexible sensor utilizes completely different sensing mechanisms of piezoresistive and thermoelectric effects to detect pressure and temperature variations, which will be beneficial to realizing the lowest cross-coupling response behavior. Therefore, the effect of temperature on the piezoresistive performance of the device is also investigated. As shown in Fig. 3f and g, whether the device is subjected to dynamically increasing stress or not, the resistance of the flexible sensor varies almost anomalously with the temperature over a wide temperature range of 0–25 K, and the resistance of the device tested under a continuous constant stress of 0–100

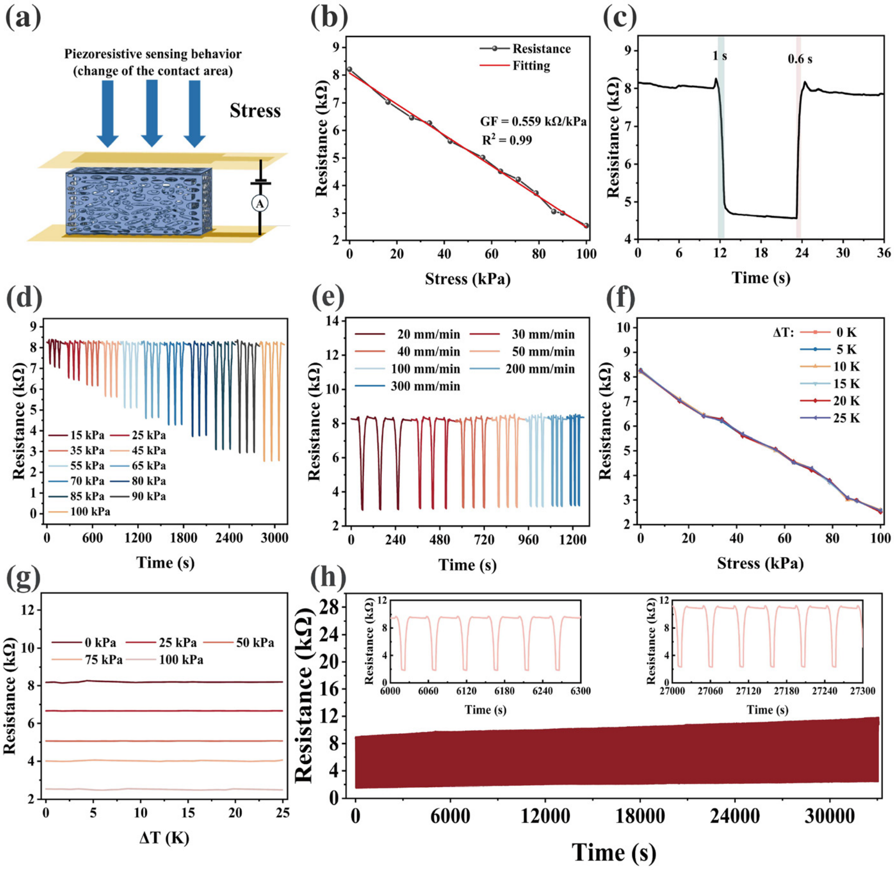

Fig. 3 Piezoresistive sensing performance of the flexible sensor. (a) Schematic diagram of the piezoresistive response mechanism. (b) The relationship between the resistance of the device and the stress applied. (c) The response and recovery times of the sensor. The piezoresistive sensing performance of the flexible device at (d) different stresses of 0–100 kPa, and (e) various compression speeds under a constant stress of 100 kPa. (f and g) Plots of the influence of temperature on the piezoresistive behavior of this device. (h) The stability of the flexible device after being cycled more than 800 times under a constant stress of 100 kPa.

kPa hardly varies with the temperature, which fully confirms that the piezoresistive performance is affected by the temperature infection in a negligible way. Moreover, a long-term cycling compression experiment is conducted under an external stress of 100 kPa to verify the fatigue resistance of the flexible sensor (Fig. 3h), showing good stability after more than 800 cycles. In a word, this melamine sponge-MXene@$CsPbBr_3$ aerogel-derived flexible sensor demonstrates good piezoresistive sensing performance without temperature interference.

2.4 Thermoelectric sensing characteristics of the flexible sensor

Furthermore, in addition to the piezoresistive property, the flexible tactile sensor has the capability of thermoelectric sensing. A unique feature of this study is that the composite of $CsPbBr_3$ can synchronously enhance the conductivity and thermoelectric coefficient of the final product, thus achieving an efficient output for thermoelectric sensing (Fig. 2a). This can be ascribed to the intrinsic semi-conductive feature of the thermal field exciting carrier's behavior; as a result, more carriers participate in the formation of the built-in ion field, outputting enhanced thermoelectric voltage. Based on the Seebeck effect, the thermoelectric open-circuit voltage is calculated using the following eqn (2):

$$\Delta U = S_T \times \Delta T \quad (2)$$

where S_T is the Seebeck coefficient and ΔT is the temperature gradient. Thus, as shown in Fig. 4a, due to the thermoelectric feature of this melamine sponge-MXene@$CsPbBr_3$ aerogel, when ΔT is applied, the thermal diffusion of the thermoelectric carriers is significantly enhanced, yielding a significant output voltage in the temperature range of ΔT = 0–25 K that covers commonly used conditions, as shown in Fig. 4b. In addition, the response time of the device is tested at ΔT = 25 K (Fig. 4c), and its response and recovery times are 4.3 s and 33.2 s, respectively. More importantly, to investigate the lack of interference between applied force and the temperature response behavior, the thermoelectric voltage of this flexible sensor is measured under various applied external pressures (Fig. 4d, temperature difference is fixed when gradually increasing external pressure) and several constant pressures (Fig. 4e, fixing external pressure applied to the device and varying the temperature difference) in arbitrary conditions, all showing unchanged output trends, which indicates that the output signal is intrinsically insensitive to changes in the applied force. Furthermore, the thermoelectric cycling stability is also tested under more than 1000 cycles at a temperature difference of 20 K, demonstrating its excellent thermoelectric sensing stability (Fig. 4f). In a word, considering together with the piezoresistive properties described above, there is no significant mutual cross-coupling response behavior between the temperature and pressure responses, further validating the multifunctional interference-free sensing capability of this melamine sponge-MXene@$CsPbBr_3$ aerogel-derived flexible sensor.

2.5 Light-sensing behavior of the flexible sensor

Based on the ultraviolet excited PL property of the melamine sponge-MXene@$CsPbBr_3$ aerogels as revealed in Fig. 2f, the photoelectric current is employed to quantitatively analyze the

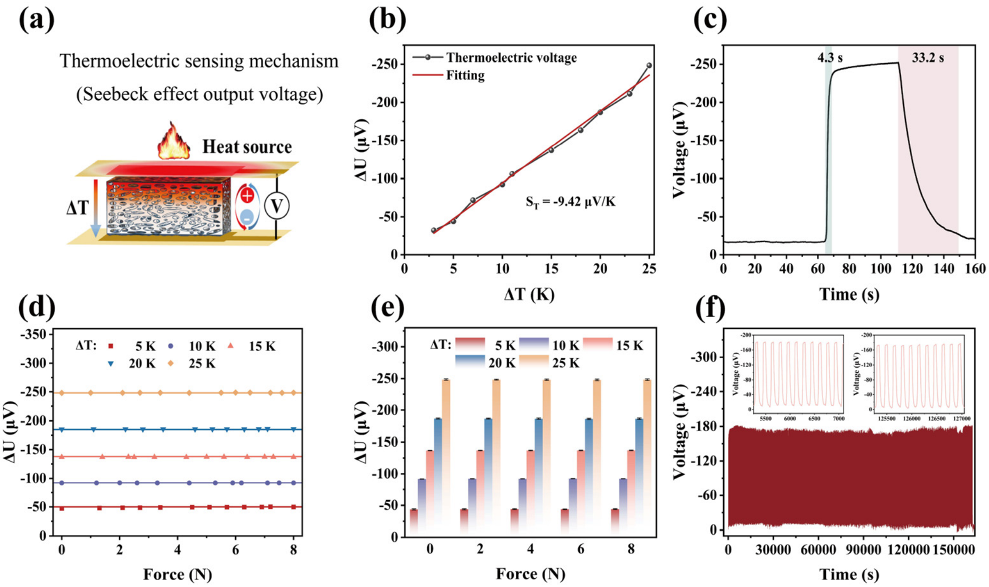

Fig. 4 Thermoelectric sensing performance of the sensor. (a) Schematic diagram of the thermoelectric response mechanism of the melamine sponge-MXene@$CsPbBr_3$-based flexible sensor. (b) The output voltage of the flexible sensor at various temperature differences. (c) The response and recovery times of the device when the temperature difference is 25 K. The output voltages of the flexible device obtained (d) under an external temperature difference by fixing the pressure, as well as (e) under external pressure by fixing the temperature difference. (f) The stability of the flexible sensor when cycled more than 1000 times under a temperature difference of 20 K.

This journal is © The Royal Society of Chemistry 2025

light response behavior of this aerogel-derived flexible sensor. For instance, when the device is irradiated by a UV light source as displayed in Fig. 5a, as well as emitting the visible green light, the electron–hole pairs are generated in the hybrid aerogel due to the photoelectric effect, which will be rapidly separated and collected by the relative electrodes under the action of an applied electric field (−5–5 V). Thus, this passive optoelectronic output can effectively be employed to quantify the light-sensing behavior. As shown in Fig. 5b and c, it can be seen that the flexible sensor indeed demonstrates favorable light-sensing behavior, not only covering from the ultraviolet to visible light bands, but also achieving nearly linear response behaviors and the highest output photoelectric current (Fig. S9, 6.74×10^{-7} A, switching ratio $>10^2$, under the same luminous power of about 84 mW cm^{-2}, a fixed distance of 3 mm) for the UV radiation band (365 nm), indicating its optimal UV responsive performance. In addition, the influence of temperature and pressure stimuli on the ultraviolet sensing outputs were also investigated under 100% irradiation intensity of the 365 nm band—the as-anticipated non-interference response ability shown in Fig. S10 and S11—which is due to the independent sensory mechanism. For the ultraviolet excited photoluminescence, the device shows a response time of 120 ms when it emits green light under UV light (Fig. 5d), and when the UV light is withdrawn, the green light disappears within 65 ms.

To verify the color quality of the green light produced by the device under UV light, such as the saturation and hue, the CIE Chromaticity Chart (introduced by the International Commission on Illumination) is used to evaluate the quality of the color by mapping the hue and the degree of package fit of colors that are visible to the human eye. The green light emitted from this sensor is plotted on the CIE chromaticity coordinates (Fig. 5e), showing that the device emits pure and well-saturated green light with a wavelength of 533 nm under UV light. More importantly, in order to verify the limiting distance of the UV sensing, the UV radiation photocurrent outputs are tested at different distances (from 1 cm to 20 cm at a fixed power of about 84 mW cm^{-2} and an applied electric field of 2 V), as shown in Fig. 5f, displaying an obvious response signal as far as 20 cm away. In brief, this melamine sponge-MXene@CsPbBr$_3$ derived aerogel flexible sensor demonstrates favorable light-sensing properties, especially the ultraviolet excited PL behavior, which can be successfully quantitatively analyzed by the photoelectric current. Together with the above mechanism of piezoresistive pressure sensing and thermoelectric temperature detecting, the derived flexible tactile sensor realizes multimodal response to pressure, temperature and light, especially the visual UV excited PL, with highly decoupled sensing capacity.

2.6 The application of the multimodal flexible sensor

Benefitting from the mutually non-interfering piezoresistive, thermoelectric, and light responsive behaviors, this multimodal flexible sensor is integrated into the finger of a human-nature robot to demonstrate the practical application. Firstly, based on the pressure and thermoelectric sensing mechanism, the hardness and material recognition capacity are tested on commonly used automobile parts. The mechanism of hard-

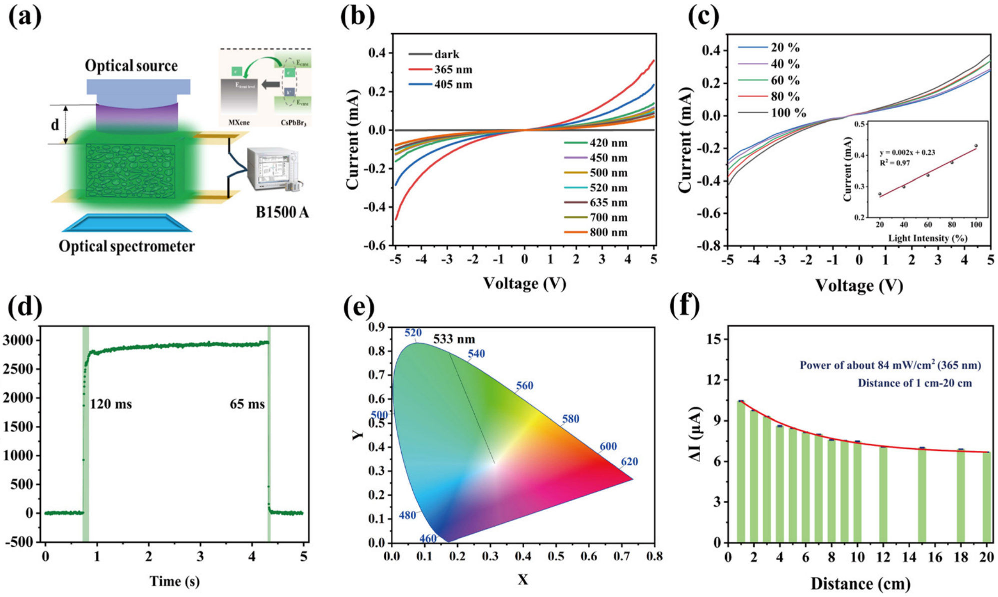

Fig. 5 Light-sensing behavior of the flexible sensor. (a) Schematic diagram of the photoelectric current mechanism of this aerogel-derived flexible sensor. The current–voltage curves of the sensor under (b) various light bands and (c) different intensities of 365 nm UV radiation, respectively. (d) The luminous response and recovery times of the flexible sensor. (e) The ultraviolet excited PL emission from the flexible sensor plotted on the CIE chromaticity coordinates. (f) The response capacity of the device at different distances under the UV radiation of 365 nm with a fixed power of about 84 mW cm^{-2} at 2 V.

ness recognition is as follows: when the robotic finger integrated with the sensor touches objects of different hardness in the same state (under the same downward movement distance that caused 100 kPa on the alloy sample as a standard point), the pressure acting on the device will be different, which will lead to differences in the output signals. For example, the harder the object is, the more force is exerted on the sensor, resulting in a greater change in resistance. Therefore, these different features are extracted for hardness recognition of objects using machine learning algorithms, which is a power-

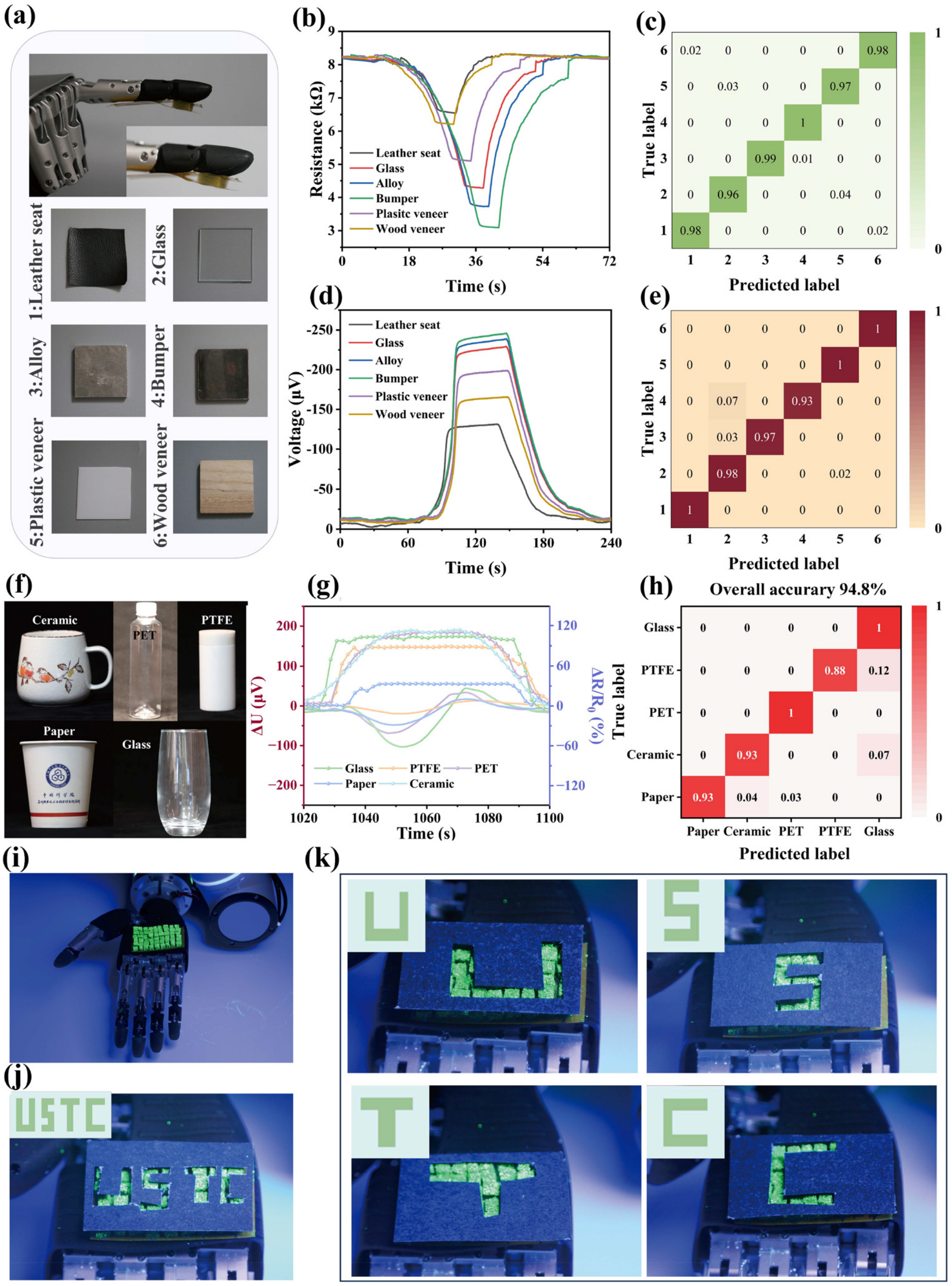

Fig. 6 The application of the multimodal flexible sensor. (a) Practical images of the robotic finger integrated with the sensor for hardness and material recognition of six objects. (b) Comparison of the induction waveforms when the device touches objects with different hardness. (c) Confusion matrix results for hardness recognition *via* the decision tree pattern. (d) Comparison of the output voltage waveforms of the sensor for objects with different materials at the same temperature. (e) Confusion matrix results obtained from the decision tree model for material recognition. (f) Optical images of objects simultaneously possessing different shapes and materials. (g) The bending piezoresistive and thermoelectric output signals for these objects. (h) The recognition accuracy *via* the dual-mode fusion algorithm. (i) Image of a robotic hand integrated with a sensor array. (j and k) The recognition results for the objects, which have been classified before *via* the hardness and material recognition, with the various shapes of "USTC", and the components with different characters of "U", "S", "T" and "C" under UV radiation.

ful tool for sensitively recognizing and classifying small differences in curves. Here, six common automobile parts (leather seats, glass, bumpers, door alloys, plastic trim, wood trim) are selected for hardness recognition, as shown in Fig. 6a. When processing the recognition data, the flexible sensor touches each type of object 100 times for a constant time (8 s) and records a large amount of data at a frequency of 10 Hz. To better compare individual data, the peak of the curve is used as a reference point, and the first 30 s and the second 42 s of the data are intercepted so that the total duration of each time series was 72 s, as shown in Fig. 6b; subsequently, 1000 identical time series data are collected for each type of object. The dataset is then divided into 800 training sets and 200 test sets. Finally, the flexible sensor achieves a high recognition accuracy of 98.2%, as shown in the confusion matrix of Fig. 6c. Furthermore, a real-time rapid aging condition was established, as displayed in Fig. S12, using a temperature and humidity aging chamber and an ultraviolet light, and this sensor can detect the hardness of objects in the various aging stages.

Based on the thermoelectric responsiveness, the device is also employed to demonstrate a human-skin-like function for material recognition, since different types of materials feel different on the skin because the thermal conductivity of individual materials varies greatly. For example, metals are good thermal conductors, and skin in contact with metals will feel colder or hotter than skin in contact with other materials at the same temperature. Inspired by this, the open-circuit voltage variation caused by nonstationary heat conduction is closely related to the thermal conductivity of the material, which can be demonstrated to distinguish between different substances.[13,14] Here, the same six materials described above are also used. The robotic hand integrated with the sensor is controlled to touch each of the materials at the same temperature, and the above machine learning is also used to help the device recognize the materials. Here, the device touches each material 100 times for a fixed time (50 s) and records a large amount of data at a frequency of 2 Hz. To better align the individual data, the first 150 s and the second 90 s of the data are intercepted using the peak of the curve as a reference point, such that the total duration of each time series data point used for training is 240 s, as shown in Fig. 6d. As an interval-based classifier, a decision tree classifier is chosen to learn the features embedded in the data. The final average accuracy reaches as high as 98.6%, as shown in the confusion matrix in Fig. 6e.

To further highlight the decoupled pressure-thermal sensing capacity of this flexible tactile sensor in the practical application, a multimodal sensing strategy using the piezoresistive signals and thermoelectric outputs is employed to classify five other complex types of objects possessing various shapes and materials simultaneously, as shown in Fig. 6f. The fused dual-signal dataset (Fig. 6g) was then input into a convolutional neural network (CNN) for classification and inference. The fused multimodal signals exhibit distinct, sample-specific response profiles. A comparison of three classification approaches, including multimodal fusion, piezoresistive-only and thermoelectric-only, demonstrates the superiority of the fused system. As shown in Fig. 6h, the dual-mode way exhibits rapid convergence during training and ultimately achieves an ultra-high classification accuracy of 94.8%, significantly outperforming the thermoelectric-only (74.2%, Fig. S13a) and piezoresistive-only (75.2%, Fig. S13b) modes, convincingly demonstrating the practical application potential of the bimodal decoupling behavior to improve recognition accuracy. Simultaneously, as well as the hardness and material recognition described above, the independent optical perception characteristics allow the sensory array to be used to distinguish the shape of small objects (Fig. S13c and d). In detail, the visual ultraviolet (365 nm) excited PL capability is described to verify the shape recognition ability. As shown in Fig. 6i, it clearly shows the PL behavior of the sensor array (9 × 6) integrated in the palm of the robotic hand when placed under UV radiation. Then, objects with different shapes, which have been classified before *via* hardness and material recognition, are approached to the array under UV irradiation. The flexible sensory array can recognize the shapes and sizes by mapping the specific response of each unit as shown in Fig. 6j. In detail, from the luminescent images and mapping results (Fig. 6k), the objects with shapes of "USTC", "U", "S", "T" and "C" can be recognized clearly, which is of great significance for robots to replace humans in the processing of automotive parts. Briefly, to delineate the novelty of this work, a comparison with recently published studies is displayed in Table S1, showing the optimal comprehensive performance of this multifunctional flexible sensor.

3 Conclusion

In this study, a melamine sponge-MXene@$CsPbBr_3$ hybrid aerogel is prepared, in which the melamine sponge provides the substrate skeleton, the MXene realizes the pressure and thermoelectric sensing functions, and the $CsPbBr_3$ achieves the light-responsive behavior, especially the ultraviolet-excited PL property. The different sensing mechanisms mean that the aerogel-derived flexible sensor can sense external variations of pressure, temperature and light, especially UV radiation, without any cross-coupling. Subsequently, this flexible sensor is employed to recognize the hardness and material of six common automotive parts through a machine learning algorithm, achieving high recognition accuracy of 98.2% and 98.6%, respectively. Finally, a sensor array is assembled to realize the shape recognition capacity. It can be envisioned that this flexible sensor based on the melamine sponge-MXene@$CsPbBr_3$ aerogel can provide accurate haptic information for human-nature robots, maximizing the replacement of humans working in complex environments.

4 Experiments and methods

4.1 Materials

Hydrochloric acid (HCl, 37%), toluene (≥99.5%), dimethyl sulfoxide (DMSO, ≥99.5%) and Ti_3AlC_2 MAX phase (500 mesh) were purchased from Sinopharm (China). Octadecylamine (90%) was purchased from Macklin (China). Cesium bromide (CsBr, 99.9%), lead bromide ($PbBr_2$, 99.99%) and acetic acid (HAc, 99.8%) were provided by Aladdin (China). Melamine sponge was purchased from Feng Tai nanomaterials Co., Ltd. All the materials were used as received.

4.2 Synthesis of MXene

MXene ($Ti_3C_2T_x$) was synthesized by etching the Ti_3AlC_2 MAX phase with LiF/HCl solution. Typically, LiF (8 g), HCl (75 mL, 9 M) and deionized (DI) water (25 mL) were mixed in a Teflon vessel with stirring under an ice bath to ensure the dissolution of LiF. To etch its Al layer, Ti_3AlC_2 powder (5 g) was slowly added to the LiF solution, and the reaction lasted for 48 h at 40 °C under stirring. The resulting Ti_3AlC_2 was repeatedly washed with water and centrifuged at 3500 rpm for 15 min until the pH value of the supernatant was above 6. Then, the supernatant was collected by centrifugation at 12 000 rpm for 30 min to collect the single-layer Ti_3AlC_2 product, and finally it was collected by freeze-drying pretreatment.

4.3 Synthesis of $CsPbBr_3$

$CsPbBr_3$ was synthesized by mixing a DMSO solution of $PbBr_2$/CsBr and a HAc solution of octadecylamine with toluene. Typically, 14 mL of dimethyl sulfoxide (DMSO) was placed in a reagent bottle, and 0.42 g of CsBr and 0.37 g of $PbBr_2$ were added to it, then the mixture was stirred thoroughly until completely dissolved. Next, 10 mL of acetic acid (CH_3COOH, HAc) was placed in a reagent bottle, and 2 g of octadecylamine was added, and the mixture was stirred thoroughly until completely dissolved. Subsequently, 0.15 mL of the above CsBr/$PbBr_2$ solution was added to 1 mL of the octadecylamine/HAc solution, and the precursor was stirred for 15 min, then 15 mL of toluene was added. The above solution was centrifuged at 5000 rpm for 5 min, and the precipitate of $CsPbB_3$ nanosheets was finally collected, then washed with toluene and vacuum dried at 70 °C.

4.4 Preparation of melamine sponge-MXene@$CsPbBr_3$ aerogel

First, 14 mL of DMSO was placed in a reagent bottle, and 0.42 g of CsBr and 0.37 g of $PbBr_2$ were added to it, and the mixture was fully stirred and dissolved. Next, 10 mL of HAc was placed in a reagent bottle, and 2 g of octadecylamine was added to it, and the mixture was fully dissolved for use. Then, 1 mL of octadecylamine/HAc solution and 0.15 mL of CsBr/$PbBr_2$ solution were added to 10 mL of MXene toluene suspension (5 mg mL^{-1}), and the mixed solution was centrifuged at 5000 rpm for 5 min after sufficient stirring for 20 min, and the precipitates were washed with toluene. The desired MXene@$CsPbBr_3$ composite was obtained after centrifugation and vacuum drying at 70 °C. Subsequently, the composite was dispersed in toluene solvent by ultrasonication (10 min) to form a homogeneous slurry, and porous diamine sponges cut into fixed sizes were repeatedly immersed in the slurry, and then placed in an oven at 70 °C for drying for 20 min. During the drying process, the rectangular porous diamine sponges were flipped over at intervals of 3 min to ensure the uniformity of the immersion; the immersion and drying process was repeated five times. Finally, the flexible copper electrodes (thickness of 18 μm) were printed on a flexible polyimide (PI) substrate (thickness of 12.5 μm) using standard flexible printed circuit methods, and then adhered to the ends of the three-dimensional sensitive materials through conductive silver paste to assemble the required flexible sensor.

4.5 Measurement and characterization

XRD patterns were recorded with a SmartLab SE diffractometer (Cu Kα radiation, λ = 0.154 nm, 40 kV, 40 mA). The microstructures of the aerogels were observed with a Hitachi S-4800 SEM, a Tecnai G2 F20 S-TWIN TEM and a FEI Quanta FEG 250 FE-ESEM. Surface structures were characterized using a Nicolet iS50 FTIR spectrometer. The chemical compositions of the aerogels were examined using a Thermo ESCALAB 250XI XPS. The compressive properties were tested using an Instron 3365 universal testing machine. PL, UV-vis and UPS tests were performed using a transient/steady-state fluorescence spectrometer (Edinburg, FLS980), a UV-visible spectrophotometer (Platinum Elmer, Lambda 650), and an ultraviolet photoelectron spectrometer (Thermo ESCALAB 250Xi), respectively. The relevant data for the UV radiation sensing test were obtained using a spectrometer (Weihai Optics, USB 2000+) and a semiconductor parameter tester (Agilent, B1500A).

To test the pressure-sensing properties of the sensor, we constructed a testing system, consisting of a pressure test bench (MARK-10, ESM303), an electric pressure gauge (MARK-10, M5–10) and the multifunctional flexible tactile sensor. We placed the sensor at the bottom of the test bench and moved the electric pressure gauge vertically toward the surface of the device. Varying pressure magnitudes were applied to the sensor by changing the moving distance of the electric pressure gauge. Meanwhile, we used a digital source meter to collect the real-time resistance variation values across the device under different pressures.

To test the thermoelectric sensing properties of the sensor, we constructed a testing system, consisting of a pressure test bench (MARK-10, ESM303), an electric pressure gauge (MARK-10, M5–10), a ceramic heating plate and the multifunctional flexible tactile sensor. We placed the sensor at the bottom of the test bench and moved the electric pressure gauge with the ceramic heating plate approached vertically toward the sensor (non-contacting mode *via* keeping a certain distance). At the same time, we changed the voltage of the programmable DC power supply (RIGOL, DP832A) to adjust the output temperature on the ceramic heating plate, so as to adjust the temperature difference applied to the upper and lower ends of the device. Meanwhile, we used a DC voltage signal acquisition recorder (Keithley, DAQ6510) to acquire and record data.

To verify the non-interference response characteristics between the pressure and thermoelectric sensing of the sensor, we constructed a pressure and thermoelectric dual-response testing system by using the thermoelectric sensing properties testing system. We placed the sensor at the bottom of the test bench and moved the electric pressure gauge with the ceramic heating plate attached vertically toward the surface of the sensor. Varying pressure magnitudes were applied to the sensor by changing the moving distance of the electric pressure gauge. Meanwhile, we changed the voltage of the programmable DC power supply (RIGOL, DP832A) to adjust the output temperature value on the ceramic heating plate, so as to adjust the temperature difference applied to the upper and lower ends of the device. At the same time, we used a DC voltage signal acquisition recorder (Keithley, DAQ6510) to acquire and record data.

4.6 Machine learning algorithms training

For hardness discrimination, the sensing datasets were collected by touching six different objects, including leather seats, glass, bumpers, door alloys, plastic trim, and wood trim. The contact time for each material was 8 s. Subsequently, the large amount of data was automatically divided into thousands of samples using Gaussian smoothing and peak-finding techniques. To better align individual data, the first 30 s and the last 42 s of the data were intercepted using the peak of the curve as a reference point, resulting in a total duration of 72 s for each time series data used for training. The obtained data samples were used for training (80%) and testing (20%), and labeled according to category. A decision tree algorithm was used for training, which resulted in an average accuracy of 98.2% for six objects with different hardness.

For material recognition, the sensing datasets were collected by touching above the same objects. The contact time with each material was 50 s. Similarly, Gaussian smoothing and peak-finding techniques were used to automatically divide the large amount of data into thousands of samples. To better align the individual data, the first 150 s and the last 90 s of the data were intercepted using the peak of the curve as a reference point, so that the total duration of each time series data used for training was 240 s. The obtained data samples were used for training (80%) and testing (20%), and labeled according to categories. The decision tree algorithm was used for training, resulting in an average accuracy of 98.6% for the objects with different materials.

Author contributions

Y. Cao and S. H. Deng contributed equally to this work. T. Li and T. Zhang are corresponding authors. S. H. Deng, Y. Cao and T. Li conceived the idea, designed the experiments and analyzed the data. T. Li and Y. Cao modified the content of the manuscript. T. Li and T. Zhang supervised the whole project. All authors discussed the results and commented on the manuscript at all stages.

Conflicts of interest

The authors declare no conflict of interest.

Data availability

The original datasets that support the plots within this paper are available from the corresponding authors upon reasonable request.

Supplementary information: preparation processes, characterizations, fluorescence lifetime and photoelectron spectra. See DOI: https://doi.org/10.1039/d5nr02882e.

Acknowledgements

The authors acknowledge the Jiangxi Provincial Natural Science Foundation (20224ACB212001), the National Natural Science Foundation of China (62471466), the National Science Fund for Distinguished Young Scholars of China (62125112), and the Gusu Leading Talents of Suzhou (ZXL2024378). The authors are grateful for the technical support from Nano-X Vacuum Interconnected Workstation of Suzhou Institute of Nano-Tech and Nano-Bionics, Chinese Academy of Sciences (SINANO).

References

1 R. Bao, J. Tao, J. Zhao, M. Dong, J. Li and C. Pan, Integrated intelligent tactile system for a humanoid robot, *Sci. Bull.*, 2023, **68**(10), 1027–1037.

2 H. Niu, F. Yin, E. S. Kim, W. Wang, D. Y. Yoon, C. Wang, J. Liang, Y. Li and N. Y. Kim, Advances in flexible sensors for intelligent perception system enhanced by artificial intelligence, *InfoMat*, 2023, **5**(5), e12412.

3 P. Zhu, Y. Wang, Y. Wang, H. Mao, Q. Zhang and Y. Deng, Flexible 3D architectured piezo/thermoelectric bimodal tactile sensor array for E-Skin application, *Adv. Energy Mater.*, 2020, **10**(39), 2001945.

4 Z. Rao, Y. Lu, Z. Li, K. Sim, Z. Ma, J. Xiao and C. Yu, Curvy, shape-adaptive imagers based on printed optoelectronic pixels with a kirigami design, *Nat. Electron.*, 2021, **4**(7), 513–521.

5 X. Ma, C. Wang, R. Wei, J. He, J. Li, X. Liu, F. Huang, S. Ge, J. Tao, Z. Yuan, P. Chen, D. Peng and C. Pan, Bimodal tactile sensor without signal fusion for user-interactive applications, *ACS Nano*, 2022, **16**(2), 2789–2797.

6 X. Qu, Z. Liu, P. Tan, C. Wang, Y. Liu, H. Feng, D. Luo, Z. Li and Z. Wang, Artificial tactile perception smart finger for material identification based on triboelectric sensing, *Sci. Adv.*, 2022, **8**(31), eabq2521.

7 M. Liu, Y. Zhang, J. Wang, N. Qin, H. Yang, K. Sun, J. Hao, L. Shu, J. Liu, Q. Chen, P. Zhang and T. H. Tao, A star-nose-like tactile-olfactory bionic sensing array for robust object

recognition in non-visual environments, *Nat. Commun.*, 2022, **13**(1), 79.

8 Y. Li, L. Yang, S. Deng, H. Huang, Y. Wang, Z. Xiong, S. Feng, S. Wang, T. Li and T. Zhang, A machine learning–assisted multifunctional tactile sensor for smart prosthetics, *InfoMat*, 2023, **5**(9), e12463.

9 S. Deng, Y. Li, S. Li, S. Yuan, H. Zhu, J. Bai, J. Xu, L. Peng, T. Li and T. Zhang, A multifunctional flexible sensor based on PI-MXene/$SrTiO_3$ hybrid aerogel for tactile perception, *Innovation*, 2024, **5**(3), 100596.

10 C. Du, M. Cao, G. Li, Y. Hu, Y. Zhang, L. Liang, Z. Liu and G. Chen, Toward precision recognition of complex hand motions: wearable thermoelectrics by synergistic 2D nanostructure confinement and controlled reduction, *Adv. Funct. Mater.*, 2022, **32**(36), 2206083.

11 W. Yang, H. Liu, H. Du, M. Zhang, C. Wang, R. Yin, C. Pan, C. Liu and C. Shen, Robust and superelastic spider web-like polyimide fiber-based conductive composite aerogel for extreme temperature-tolerant linear pressure sensor, *Sci China Mater.*, 2023, **66**(7), 2829–2842.

12 L. Yang, Y. Li, L. Fu, X. Shi, T. Li and T. Zhang, Flexible pressure/temperature sensing system based on Te-PEDOT: PSS composite thermoelectric material, *Sci. Sin. Technol.*, 2023, **53**(4), 487–498.

13 Y. Li, M. Zhao, Y. Yan, L. He, Y. Wang, Z. Xiong, S. Wang, Y. Bai, F. Sun, Q. Lu, Y. Wang, T. Li and T. Zhang, Multifunctional biomimetic tactile system via a stick-slip sensing strategy for human-machine interactions, *npj Flexible Electron.*, 2022, **6**(1), 46.

14 H. Yang, J. Li, X. Xiao, J. Wang, Y. Li, K. Li, Z. Li, H. Yang, Q. Wang, J. Yang, J. S. Ho, P.-L. Yeh, K. Mouthaan, X. Wang, S. Shah and P.-Y. Chen, Topographic design in wearable MXene sensors with in-sensor machine learning for full-body avatar reconstruction, *Nat. Commun.*, 2022, **13**(1), 5311.

15 F. Gao, J. Liu, X. Li, Q. Ma, T. Zhang, Z. Yu, J. Shang, R. Li and X. Li, Ti_3C_2Tx MXene-based multifunctional tactile sensors for precisely detecting and distinguishing temperature and pressure stimuli, *ACS Nano*, 2023, **17**(16), 16036–16047.

16 Z. Zhang, Y. Li, C. Liang, G. Yu, J. Zhao, S. Luo, Y. Huang, C. Su and G. Xing, In situ growth of $MAPbBr_3$ nanocrystals on few–layer MXene nanosheets with efficient energy transfer, *Small*, 2020, **16**(17), 1905896.

17 J. Hu, D. Liu, X. Xia, B. Wang, D. Pan, Y. Cheng and Y. Lu, MXene/perovskite-based bionic human odor sensor array with machine learning, *Chem. Eng. J.*, 2023, **468**, 143752.

18 Z. Yao, W. Cao, Z. Wang, L. Miao, J. Shi and R. Xiong, Anharmonic phonon renormalization and thermoelectric properties of $CsPbX_3$ (X = Cl, Br, and I): first-principles calculations, *Phys. Chem. Chem. Phys.*, 2023, **25**(38), 26236–26244.

19 H. Wang, Z. Guo, X. Pu and Z. Wang, Ultralight iontronic triboelectric mechanoreceptor with high specific outputs for epidermal electronics, *Nano-Micro Lett.*, 2022, **14**(1), 86.

20 H. Hu, Y. Ma, X. Gao, D. Song, M. Li, H. Huang, X. Qian, R. Wu, K. Shi, H. Ding, M. Lin, X. Chen, W. Zhao, B. Qi, S. Zhou, R. Chen, Y. Gu, Y. Chen, Y. Lei, C. Wang, C. Wang, Y. Tong, H. Cui, A. Abdal, Y. Zhu, X. Tian, Z. Chen, C. Lu, X. Yang, J. Mu, Z. Lou, M. Eghtedari, Q. Zhou, A. Oberai and S. Xu, Stretchable ultrasonic arrays for the three-dimensional mapping of the modulus of deep tissue, *Nat. Biomed. Eng.*, 2023, **7**(10), 1321–1334.